Combined Molecular Dynamics−Continuum Study of Phase Transitions in Bulk Metals under Ultrashort Pulsed Laser Irradiation†

W. Wendelen,‡ A. A. Dzhurakhalov,*,‡,§ F. M. Peeters,§ and A. Bogaerts‡

Research group PLASMANT, Department of Chemistry, University of Antwerp, Universiteitsplein, 1, B-2610, Wilrijk, Belgium, and Department of Physics, University of Antwerp, Groenenborgerlaan 171, B-2020 Antwerpen, Belgium

Received: July 31, 2009; Revised Manuscript Received: December 23, 2009

The phase transition processes induced by ultrashort, 100 fs pulsed laser irradiation of Au, Cu, and Ni are studied by means of a combined atomistic-continuum approach. A moderately low absorbed laser fluence range, from 200 to 600 J/m^2 is considered to study phase transitions by means of a local and a nonlocal order parameter. At low laser fluences, the occurrence of layer-by-layer evaporation has been observed, which suggests a direct solid to vapor transition. The calculated amount of molten material remains very limited under the conditions studied, especially for Ni. Therefore, our results show that a kinetic equation that describes a direct solid to vapor transition might be the best approach to model laser-induced phase transitions by continuum models. Furthermore, the results provide more insight into the applicability of analytical superheating theories that were implemented in continuum models and help the understanding of nonequilibrium phase transitions.

1. Introduction

Recently developed and commercialized femtosecond laser systems have found several industrial and medical applications.[1−4] The ultrashort pulse duration provides unique possibilities for the very precise treatment or machining of a variety of materials, including transparent dielectrics. However, in spite of the demonstrations of the high industrial potential of ultrashort laser pulses, the fundamental mechanisms of the interaction of these pulses with different materials are still subject to discussion.

Theoretical studies on this matter are usually based on a two-temperature model (TTM).[5] The laser energy is absorbed by the electrons, and then gradually passed on to the lattice by electron−phonon coupling. While attempts have been made to implement thermal heterogeneous melting, the basic two-temperature model is unable to cope with the rapid phase transitions involved in ultrashort pulsed laser ablation since the melting occurs under conditions of strong thermal nonequilibrium.[6,7]

In some continuum models, the phenomenological superheating theory of Jackson[8] is used to implement heterogeneous melting. According to his research, the melting front velocity in metals can be expressed as a function of the level of superheating. The main weakness in this theory lies within the fact that there is no limit for the level of superheating, while it is also necessary to fit a combination of two parameters to the molecular dynamics (MD) results. In addition, there are other effects, such as pressure waves caused by the lattice deformation, which could influence the melting process considerably. Therefore, the applicability of a theory solely based on a lattice temperature within continuum models should be investigated.

For the simulation of melting by homogeneous nucleation with continuum models, attempts were made using classical nucleation theory.[9−11] The assumption was made that the growth of a liquid region in a superheated solid would progress in the same way as the crystallization of a solid in an undercooled liquid. The authors pointed out that the theory is not quantitative, but rather a qualitative proof that ultrashort pulsed laser-induced melting of bulk metals could be initiated by a homogeneous nucleation mechanism. Furthermore, strong pressure gradients are created that will influence the melting process. Several attempts have been made to calculate this by means of a hydrodynamic model.[12,13] However, for this approach, accurate data are necessary for the equation of state of the solid. In brief, an accurate kinetic theory for the nucleation processes involved for rapid laser-induced melting of metals is not yet available.

Other approaches to study the rapid laser-induced phase transitions make use of MD simulations combined with a continuum description of laser excitation, electron−phonon equilibration, and electron heat conduction.[14−21] This approach employs the general two-temperature model, where the laser beam interacts directly with the top part of the lattice represented by an MD-box. Up until now, this is the preferential approach to cope with rapid phase transitions under strong nonequilibrium conditions. The drawback is that for accurate simulations of homogeneous nucleation, a very large MD-box is needed.

The goal of our MD simulations is to investigate the phase transitions that occur following ultrashort pulsed laser irradiation without making any assumptions for the kinetics of the melting process. Our results illustrate the possibilities and advantages of MD-simulations compared to continuum models to investigate the rapid laser-induced phase transitions. Calculations are performed for Au, Ni, and Cu. Ni and Au are metals with high and low values for electron−phonon coupling strength, respectively, while Cu differs from Au in density and thermal expansion coefficient.

2. Simulation Details

To simulate the interaction of an ultrashort laser pulse with metals we combine a continuum model with molecular dynamics

† Part of the "Barbara J. Garrison Festschrift".

* To whom correspondence should be addressed. E-mail: Abdiravuf.Dzhurakhalov@ulb.ac.be.

‡ Department of Chemistry, University of Antwerp.

§ Department of Physics, University of Antwerp.

10.1021/jp907385n
Published on Web 01/26/2010

simulations, similar to the combined model described in ref 14. However, there are several major differences in these two models as indicated further in the text. Here we briefly describe both the continuum model based on a TTM for studying the time evolution of the electronic and lattice temperatures, and the MD model for the atomistic study of the melting and evaporation processes, as well as the combination of both models.

TTM. The basis of the continuum approach is the TTM pioneered by Anisimov et al.[5] While the assumption of thermal equilibrium made for this approach might not be completely correct, the TTM is still widely used to model energy transport for metals under ultrashort pulsed laser irradiation. In the TTM, the time evolution of the electron and lattice temperatures is described by the following nonlinear differential equations

$$C_e(T_e)\frac{\partial}{\partial t}T_e = \frac{\partial}{\partial x}K_e(T_e, T_l)\frac{\partial}{\partial x}T_e - G(T_e)(T_e - T_l) + S_{laser} \quad (1)$$

$$C_l(T_l)\frac{\partial}{\partial t}T_l = \frac{\partial}{\partial x}K_l(T_l)\frac{\partial}{\partial x}T_l + G(T_e)(T_e - T_l) \quad (2)$$

In these equations, T_e and T_l are the electron- and lattice temperatures, K_e and K_l are the electron and lattice heat conductivities, and C_e and C_l are the electron and lattice heat capacities, respectively. G is the electron−phonon coupling parameter and S_{laser} denotes a source term that simulates the input of laser energy to the system. In most TTM studies (in particular in the mentioned ref 14), a linear electron heat capacity, electron heat conductivity, and a constant electron−phonon coupling parameter are used. However, following refs 7 and 22 for femtosecond laser irradiation it is essential to use a nonlinear electron heat capacity and a temperature dependent electron−phonon coupling parameter as in this case the resulting electron temperature exceeds T_F/π^2 (where T_F is the Fermi temperature) and becomes comparable to T_F. That is why in the present calculations we use the nonlinear $C_e(T_e)$ and $G(T_e)$ given in ref 22, which are derived from DOS calculations, and the functional for the $K_e(T_e,T_l)$ given in refs 23 and 24. For our case, the lattice heat conductivity is negligible.

MD Model. In our MD simulation, the equations of motion of the atoms in the system are integrated stepwise in time with the algorithm described in ref 25. The major parameter for MD simulations that governs the interatomic interactions in the system is of course the interatomic interaction potential. To describe properties of solids correctly, a many body potential needs to be used. For metallic systems, the potentials based on the second moment approximation of the tight binding model[26,27] and on the embedded atom method (EAM)[28,29] are currently used. We use the EAM with the functional of the electronic density suggested by Johnson[29,30] which is a bit different from the EAM one used in the mentioned ref 14. The EAM is quite convenient as it allows a choice for the range of atomic interactions. In this formalism, the number of shells and thus the range of the interactions is arbitrary. For the purpose of the present simulations, shells until the fourth neighbor distance are taken into account for the species having the largest first neighbor distance in its elemental equilibrium structure, which is Au with a lattice distance of 0.408 nm at 0 K. So, the cutoff distance in the present calculation is 0.613 nm, which includes all neighbor atoms within four neighbor shells in a perfect Au crystal, five neighbor shells in Cu, and six neighbor shells in Ni. This cutoff distance is large enough even for the case of thermal expansion at the temperatures studied.

To evaluate whether the EAM Johnson potential[30] is accurate enough to describe the thermal properties of Au, Cu, and Ni crystals, MD calculations were performed for a face-centered cubic (fcc) $6a_0 \times 6a_0 \times 6a_0$ box (where a_0 is the lattice parameter), which contains 864 atoms with 3D periodic boundary conditions. In Figure 1, the calculated and experimental[31−35] values of the thermal mean square displacements in Au, Cu, and Ni as well as their calculated lattice parameters are shown versus temperature. Notice that good agreement between theory and experiment is obtained in particular for Cu and Ni and to a lesser extent for Au. It should be mentioned that the parameters of the Johnson potential were fitted at 0 K with the lattice parameter measured experimentally at 300 K. The calculated lattice parameters at 0 K are 4.08, 3.615, and 3.52 Å for Au, Cu, and Ni, respectively. As shown in Figure 1d the lattice parameter increases with temperature because of the thermal expansion of the crystal.

Combined MD-Continuum Model. In our case a 100 fs fwhm laser pulse is directed in the z-direction and interacts with bulk metal. The simulation grid is 500 nm in length in the z-direction. The lattice was divided into two parts. The top part is represented by the MD-model coupled with the TTM because the treatment of the nonequilibrium phenomena requires an atomistic approach. However, it is not necessary to use the computationally expensive MD-method in the bulk part, defined here as the lattice region beyond the first 100 nm, hence for this part the conventional continuum model is used. Therefore it is also necessary to establish a link between these two parts of the lattice (see below).

The initial length of the MD box in the z-direction was ∼100 nm and its size corresponds to $10a_0 \times 10a_0 \times 240a_0$ for Au, $10a_0 \times 10a_0 \times 270a_0$ for Cu and $10a_0 \times 10a_0 \times 280a_0$ for Ni. The laser beam impinges on the (001) surface. The MD box has an fcc structure and contains 96 000, 108 000, and 112 000 atoms for Au, Cu, and Ni, respectively. The number of atoms in each layer in the lateral (001) plane is 200. Periodic boundary conditions were used only in the lateral x and y directions. The MD box is initially thermalized at $T = 300$ K. In this part of the lattice, eq 2 (see above) is replaced by the MD equation of motion

$$m_i\frac{d^2\vec{r}_i}{dt^2} = \vec{F}_i + \xi m_i\vec{v}_i^T \quad (3)$$

where m_i and r_i are mass and position of atom i, and $\vec{F}_i$ is the interatomic force acting on atom i. The second term on the right is the electron−phonon coupling term accounting for the energy exchange between the electrons and lattice where $\vec{v}_i^T$ is the thermal velocity of atom i. Using a tridiagonal matrix algorithm, eq 1 for the electron temperature is solved by an implicit finite volume method simultaneously with the MD integration of eq 3. Since MD-calculations are computationally more expensive than solving the continuum equations, different time steps are used for the electron and lattice subsystem. In our calculation, the electron temperature is calculated every 0.1 fs, while electron−phonon coupling is integrated over every 2 fs MD time step, to be used as input for the MD-simulation. The size of the grid cells in the z-direction in the finite difference discretization is ∼2 nm, which is related to the corresponding volume of the MD-box consisting of 2000 atoms for Au and 2400 atoms for Cu and for Ni on average for the initial MD-

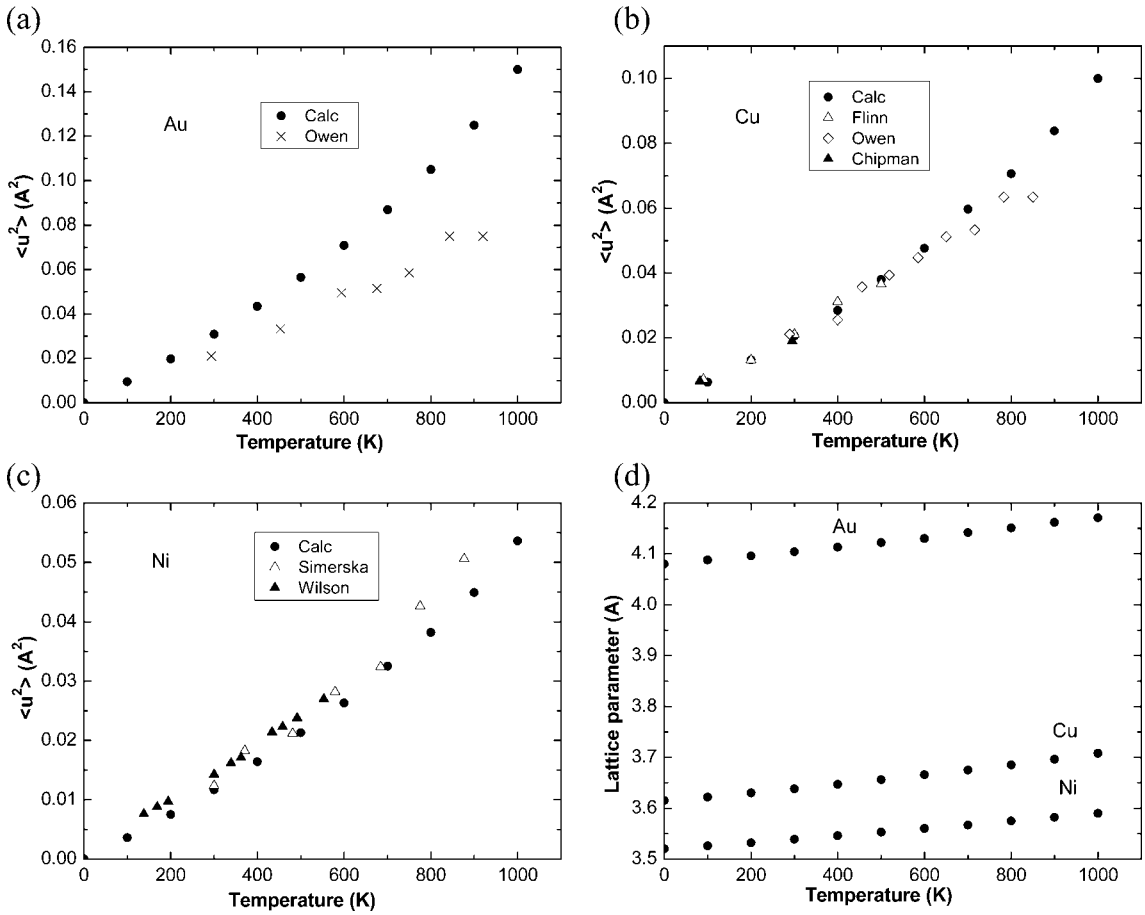

Figure 1. Mean square displacements of Au (a), Cu (b), and Ni (c) vs temperature. Calculations (Calc) were performed using the MD technique. Experimental values for Au were measured by Owen et al,[31] for Cu by Flinn et al,[32] Owen et al[31] and Chipman et al,[33] and for Ni by Simerska[34] and Wilson et al.[35] The calculated lattice parameters of Au, Cu, and Ni crystals are plotted vs temperature in (d).

lattice. The definitions of the coefficient ξ and of the lattice temperature calculated for each cell are given in ref 14. All properties are scaled according to the local atomic number density in the corresponding cell.

The top part of the lattice, represented by an MD-box, is prone to phenomena such as thermal expansion due to the lower mass density at higher temperatures. Earlier works solved this problem by keeping the reference system bound to its own position and by switching on and off cells above the target based on a density criterium.[14,15] Using this approach, a crude assumption is required for the electron temperature for adding new cells due to the gradients in electron temperature at the surface region.

To simulate for bulk metals, free boundary conditions are used for the remote boundary. This is acceptable as long as the temperature at the remote boundary remains close to 300 K. In this study, the position of the reference system of the continuum equations is moved according to the position of the top part of the lattice, which is determined by the MD-box. The coupling of the MD-box to the continuum part of the lattice is realized by introducing a moving boundary (see Figure 2a−c). The two cells at the MD-continuum boundary are separated by a moving boundary, the position of which is determined by the length of the MD-box. The MD-box starts off with a length of NB × dx (NB being an integer, dx being the length of one spatial grid cell). Whenever this length crosses a value of $(N \pm 1/2) \times$ dx, another cell is added to or removed from the continuum part (this is realized by employing $NB' = NB \pm 1$ as shown in Figure 2c), while the total number of cells remains constant. The positions of the cell centers will be shifted by $\pm 0.5 \times$ dx in this time step, which introduces some error, but since in this region the temperature gradients are considerably lower, this error will surely be smaller than the one made by adding cells in the surface region. The moving boundary used in our calculations improves the implementation of thermal expansion, compared to the model used in ref 14. The MD particles at the boundary between the MD and the continuum part are damped using Langevin dynamics[36,37] in order to avoid evaporation of particles and the reflection of the wave caused by laser heating. The length of the damped part of the MD box was chosen as ∼4 nm.

Study of the Melting Process. To evaluate whether the atoms are ordered, and hence the degree of melting, the structure factor and the local order parameter are calculated. The structure factor[38,39] is computed within a given grid cell as

$$S = \frac{1}{N}\sum_{j=1}^{N} e^{i\mathbf{k}\mathbf{r}_j} \tag{4}$$

In this expression, $\mathbf{k}$ is the wave vector, $\mathbf{r}_j$ is the position of the atom j, and N is the number of atoms in the given grid cell. If the periodicity in the direction of $\mathbf{k}$ corresponds to the inverse of $|\mathbf{k}|$, then the value of $|S|^2$ is unity. If there is no such periodicity in this direction, $|S|^2$ is zero. The wave vector is determined as

$$\mathbf{k} = \frac{4\pi}{a_0}(h, k, l) \tag{5}$$

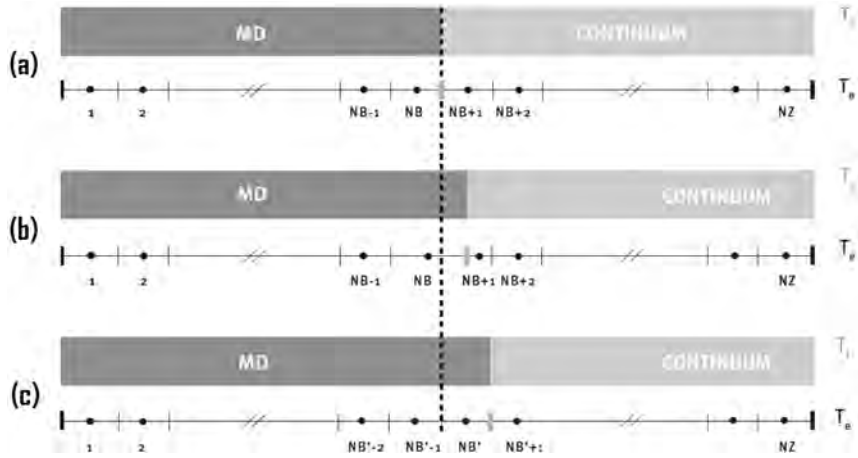

Figure 2. Schematic representation of the MD-Continuum moving boundary for different times. The dashed line shows the initial position of the boundary.

where a_0 is the lattice parameter, and h, k, and l are Miller indices of the lattice.

The local order parameter provides a measure of the local fcc order for each atom.[40] It can be defined by a set of N_k wave vectors $\{\mathbf{k}_m\}$ such that $\exp(i\mathbf{k}_m\mathbf{r}_{ij}) = 1$ for any vector $\mathbf{r}_{ij}$ connecting near neighbors in a perfect fcc lattice. The local order parameter was defined by Morris et al[40] as

$$\Psi_i = \left|\frac{1}{6}\frac{1}{Z}\sum_{j=1}^{Z}\sum_{m}^{6}\exp(i\mathbf{k}_m\mathbf{r}_{ij})\right|^2 \qquad (6)$$

where the first sum runs over each of the Z neighbors found within a cutoff distance r_{cut} from atom i, chosen in our calculation so that all atoms in the first and second neighbor shells in the perfect lattice are included.

The melting process of the irradiated metal in the MD-box is monitored by the value of the structure factor. Homogeneous and heterogeneous melting were distinguished using two possible criteria. Homogeneous melting can occur in several grid cells at the same time. This will be clearly visible when the structure factors of different cells are plotted. Furthermore, the heterogeneous melting process is about 1 order of magnitude slower than melting induced by homogeneous nucleation.

3. Results and Discussion

General Melting Mechanism. The ultrashort pulsed laser irradiation causes extreme conditions in condensed matter initially resulting in a highly nonequilibrium state as the laser energy is deposited in the electronic subsystem, while the lattice remains cold.[5] Because of heat transfer to the phonon system the lattice may be heated to very high temperatures within a few picoseconds, exceeding the melting temperature. Under moderate conditions, melting starts heterogeneously at the surface (where the energy barrier for heterogeneous nucleation at the solid−vapor interface is almost zero) and consequently a melt front propagates from the surface into the material.[41] However, experiments[42] and MD calculations[14,43,44] indicated that homogeneous volumetric melting, that is, the homogeneous nucleation and growth of liquid regions inside the overheated crystal, also occurs during femtosecond laser ablation. In ref 14, it is shown for thin Ni and Au films that the dominant nucleation mechanism for melting of thin metal films can either be heterogeneous or homogeneous. However both processes may always be occurring. These mechanisms mainly depend on the laser fluence, pulse duration, and the strength of the electron−phonon coupling parameter of the material.

Several questions might arise when studying the melting processes by MD-calculations, such as when exactly can we consider a material as molten, what is the most objective way to describe a melting front, what is the melting temperature in conditions observed after ultrashort pulsed laser ablation, and so forth. In this paper, a qualitative analysis is made of the general melting process. This has been done grid cell-by-grid cell using a structure factor (as in ref 18 where it was done

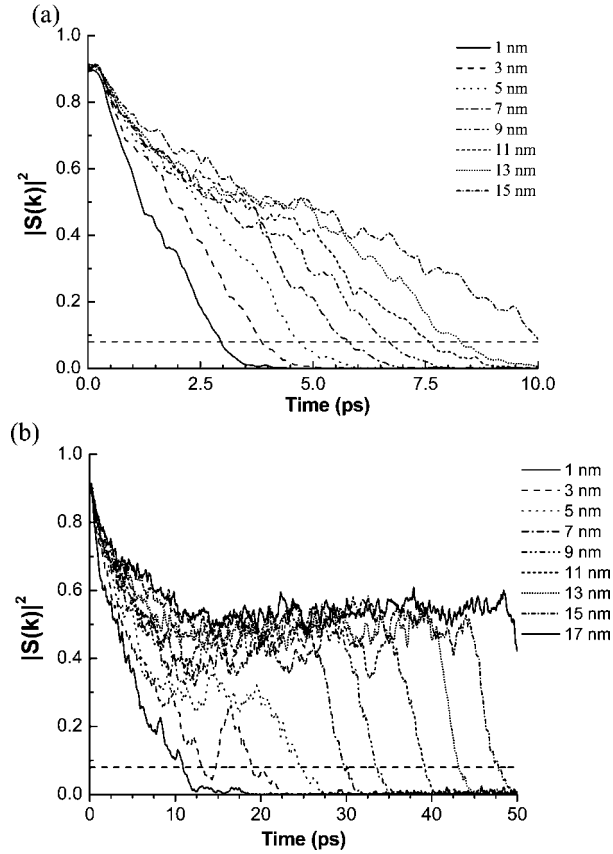

Figure 3. Temporal evolution of the structure factor $|S(k)|^2$ calculated for the (001) plane in different grid cells (i.e., different depths in the target) for an absorbed fluence of 400 J/m^2 (a) and 250 J/m^2 (b) for Au. The dashed horizontal line corresponds to a structure factor of 0.08, which is used as the threshold value for the liquid state of the material.

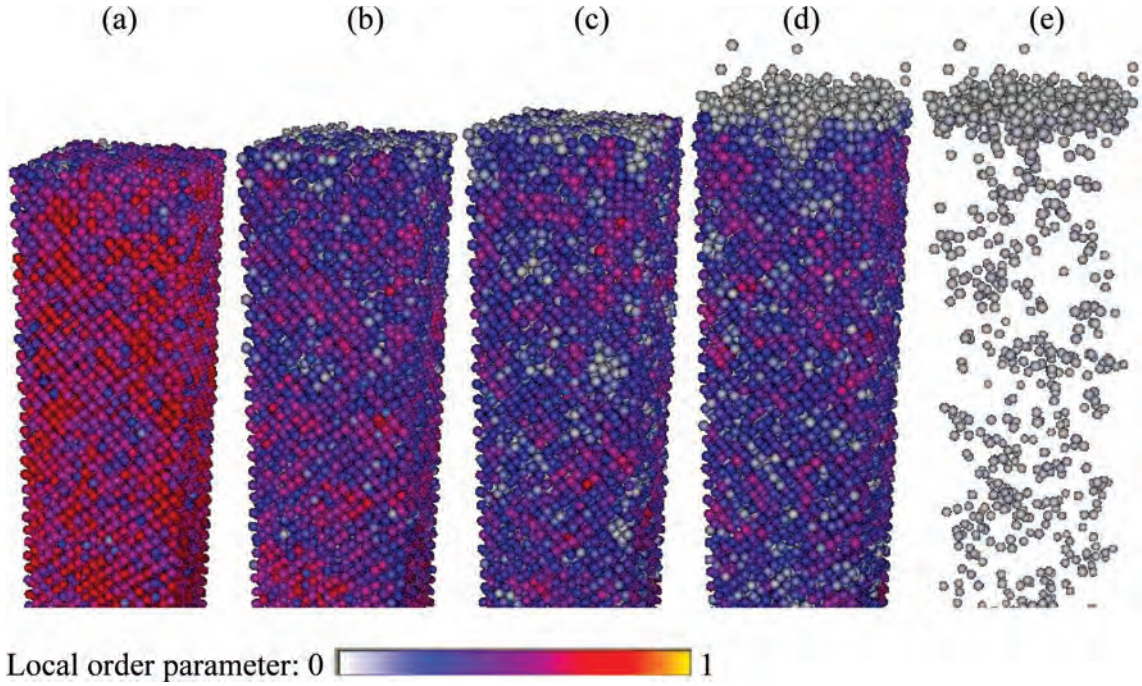

Figure 4. Real space representation of the position of the Au atoms and the corresponding local order parameter for an absorbed fluence of 255 J/m^2 after 1, 3, 5, and 9 ps [(a−d), respectively], and showing only the liquid atoms after 9 ps (e).

layer-by-layer) to provide a qualitative view of the melting processes, and atom-by-atom using a local order parameter for a more detailed calculation of the melting front. The concept of a melting front is in fact more a necessity for continuum simulations, than a realistic representation of the melting process. In fact, melting happens, as mentioned above, either by propagation of a melting front in a heterogeneous process, or spread out over a larger area by homogeneous nucleation of liquid regions in the superheated lattice.

The calculation of the actual melting temperature involves some arbitrariness, since it is position dependent and involves an averaging over some region. This complicates the search for an analytical relation between melting temperature and melting front velocity.

For high-fluence ultrashort pulsed laser irradiation of metals, it is found that melting occurs via a combination of homogeneous and heterogeneous nucleation. In the early stage, liquid regions are formed in the material in front of the actual melting front, leading to an apparent melting front velocity of about 1000 m/s measured experimentally in semiconductors.[45] After some 10−30 ps or longer,[14] a purely heterogeneous melting process can be identified. A clear melting front propagates with velocities up to some 100 m/s. This melting process can be observed qualitatively in Figure 3 as the temporal evolution of the static structure factor $|S(k)|^2$ versus time for Au for a 100 fs fwhm pulse of two different absorbed laser fluences. We have varied the threshold values of $|S(k)|^2$ from 0.08 to 0.3 for distinguishing liquid from solid, and it gave almost the same results. We used the smallest threshold value in our calculation as this is the most severe criterion.

It is clear from Figure 3a that for a laser fluence of 400 J/m^2, the melting process is initiated by homogeneous nucleation, since it occurs in several atomic layers at the same time. This can be deduced from the value of the structure factor at different depths in the MD-box, which decreases in several cells at the same time. After 7.5 ps, 5 cells have molten, which means a melting front velocity of approximately 1400 m/s, indicative indeed for homogeneous melting. The melting process will proceed by heterogeneous melting at later times. For a laser fluence of 250 J/m^2, shown in Figure 3b, the melting process is also initiated by homogeneous nucleation, but it is clear that at 30 ps, a heterogeneous melting front propagates through the material, since the structure factor at different depths decreases in a stepwise manner. A melting front velocity of 300 m/s can be deduced, since 2 nm melts in 7 ps.

The melting process in real space is illustrated in Figure 4. The figures show the evolution of the distorted lattice in the first 9 ps. Although in general it can be deduced that gradually more atoms are found in the liquid state, the concept of a clear visual difference between the liquid and solid state is quite hard to make. Atoms appear showing a broad range of values for the structure factor, so a cutoff value should be used. Furthermore, from Figure 4e it is clear that a melting front is a very crude representation of the actual physical process, because the liquid atoms do not only appear at the surface region, but are also spread out deeper inside the material, that is, there is no clear interface between the solid and the liquid as shown also in ref 46. This is the reason why an approximation has to be made, if melting is implemented in continuum models.

An exact position of the laser-induced melting front is not useful to calculate the melting front velocity due to problems concerning the reference system. If the melting front position is defined relative to the top of the lattice, this reference would be faulty because it would shift during evaporation. On the other hand, if an absolute position is defined (e.g., relative to the bulk-continuum boundary), this is prone to thermal expansion. In this way during the melting process, the melting front can move upward because thermal expansion occurs at a faster rate than heterogeneous melting. In order to test the phenomenological theory of Jackson,[8] we counted the number of atoms in the solid state to represent the position of the melting front, as it is the most objective property to describe the amount of molten material (see below).

Evaluation of Phase Transitions. As mentioned above, simulations have been performed for 3 different materials: Au, Cu and Ni. For each material, the laser-induced phase transitions

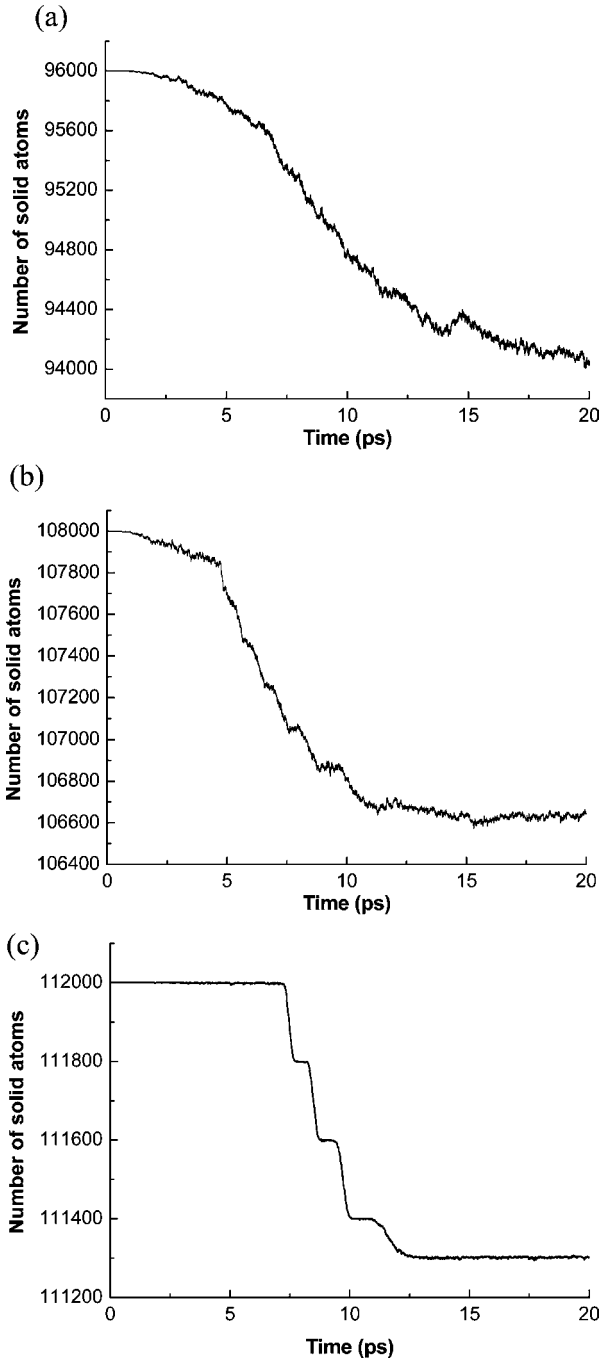

Figure 5. Number of atoms in the solid state for an absorbed fluence of 250 J/m^2 in Au (a), Cu (b), and Ni (c). The total number of atoms in the three cases is 96 000 (Au), 108 000 (Cu) and 112 000 (Ni).

were investigated for a certain range of absorbed fluence. For Au and Cu this fluence range was from 200 to 400 J/m^2 and for Ni from 200 to 650 J/m^2. It was observed that in the fluence range of 200−260 J/m^2, most of the melting occurs heterogeneously, although for Au and Cu, due to the lower electron−phonon coupling factor and higher conductivity, homogeneous melting did occur at early times. The melting front evolution is illustrated in Figure 5 for an absorbed fluence of 250 J/m^2 for Au, Cu and Ni by plotting the number of atoms in the solid state versus time.

The decrease in solid atoms is caused by both melting and evaporation. It occurs after approximately 7 ps for Au and Ni, and after approximately 4 ps for Cu. A stepwise evolution of the number of solid atoms is observed for all these three metals,

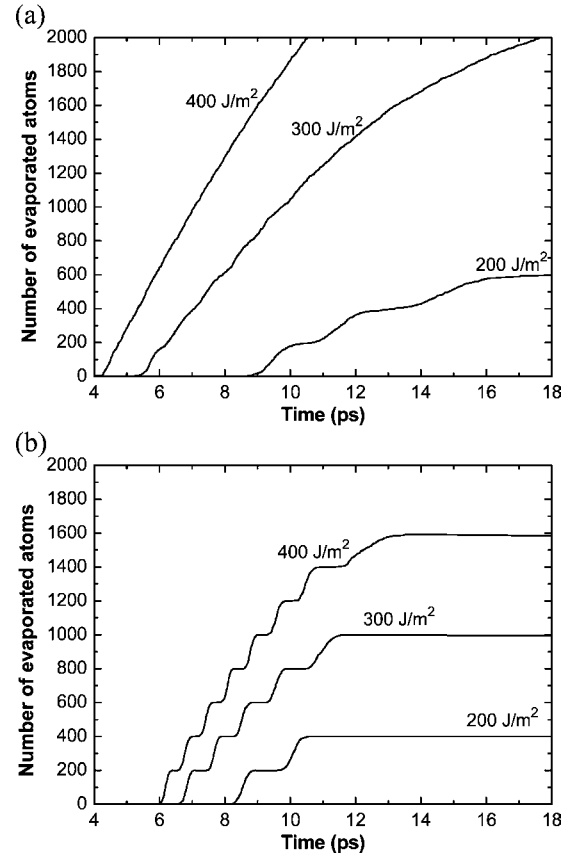

Figure 6. Time evolution of the number of evaporated atoms for Au (a) and Ni (b) for different absorbed fluences. The total number of atoms in the case of Au is 96 000 and it is 112 000 for the case of Ni. The results for Cu (not shown) are very similar to the ones for Au.

but it becomes more obvious for Cu and Ni. To understand the nature of this stepwise evolution, it is necessary to make a clear distinction between the three phases (solid, liquid, vapor) based on the local order parameter (see above). Although this radical view is not completely realistic, it is the best way to analyze the phase transitions.[40] A value of the local order parameter $\Psi_i = 0.04$ is used in this study to distinguish between the liquid and crystal phase. A criterion for vapor atoms is a value of $\Psi_i = 0$. The number of vapor and liquid atoms based on this criterion is plotted versus time for Au and Ni in Figure 6 and 8, respectively, for different values of the absorbed fluence.

It is clear from Figure 6 that in the case of Au at 200 J/m^2 the stepwise evolution of the number of solid atoms (as shown in Figure 5) can be attributed to the vaporization; evaporation indeed occurs layer-by-layer as each layer consists of 200 atoms (see above). The atoms of the surface layer always evaporate after some delay. This demonstrates that it is necessary for the atoms in a layer to gain enough energy over time in order to evaporate (as will be illustrated below). Analysis of the local order parameter shows that for Au at 200 J/m^2 during the first 9 ps some atoms are molten within 60−70 layers. Although most of the molten atoms occur in the surface layer, their number is less than 50% of the total number of atoms in this layer. So, the surface layer is not fully molten.

For higher fluences (300 and 400 J/m^2) in the case of Au, a stepwise behavior for evaporation is not observed as several layers are molten simultaneously and evaporation of atoms occurs from the molten part of the crystal. A similar behavior of the time evolution of evaporation at three considered laser fluences was observed for Cu too (not shown).

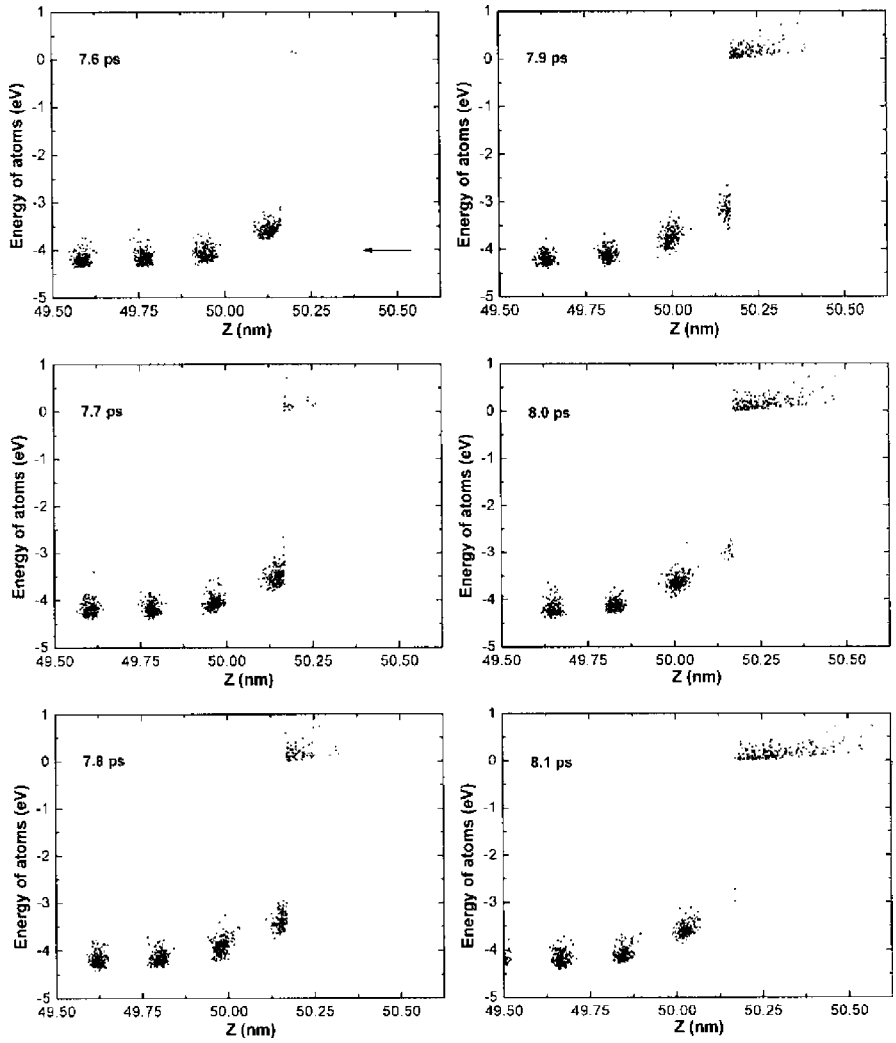

Figure 7. The time evolution of energy of surface and subsurface atoms (as defined by their positions in the *z*-direction) for Ni at 230 J/m^2. The arrow at 7.6 ps indicates the direction of the laser beam. The MD box with initial 100 nm length is centered in its middle in the *z*-direction.

However, a different mechanism is observed for Ni. As it is seen in Figure 6b, evaporation occurs by a kind of layer-by-layer mechanism for all three fluences. In this case the amount of liquid atoms formed is very limited; only 10% of the surface atoms is in the liquid state. In the case of Ni, such stepwise dependence is observed in the entire range of fluences studied for this paper (until 650 J/m^2).

The detailed evaporation process of the Ni surface at an absorbed laser fluence of 230 J/m^2 is presented in Figure 7 by plotting the energy of the surface and subsurface atoms versus their positions. Note that the lattice subsystem (in particular also its surface layer) is continuously gaining energy from the electron subsystem. In this case, the surface layer has gained enough energy after 7.6 ps, so that evaporation of the surface atoms can start. There are four layers in the diagram at 7.6 ps, shown by the positions of the atoms in the z-direction. The right group of dots indicates the atoms in the surface layer. The arrow indicates the direction of the laser beam. When time progresses (see at 7.7, 7.8 ps, and so on) this right group of dots will gradually jump to the top, and form a new group of dots at about 0 eV, indicating the evaporated atoms. For Ni the binding (cohesive) energy per atom is 4.45 eV/atom at 0 K. The cohesive energy of an atom is directly related to the thermal energy required to free the atom from the solid. Besides it is well-known that as surface atoms have fewer neighboring atoms in close proximity compared to atoms in the bulk of the solid, they bind to the solid phase with less cohesive energy. That is why the average energy of the surface atoms is somewhat higher (i.e., less negative) than for the other layers (see Figure 7 at 7.6 ps). Because of the laser absorption, atoms are gaining energy that is sufficient for breaking the bonds with the other atoms, leading to evaporation. When evaporation starts, the cohesive energy in the surface layer becomes lower as the surface layer is not complete anymore, or in other words, atoms remaining on the surface have fewer neighbors than before the onset of evaporation of the layer. The time evolution of evaporation of surface atoms shows that it occurs atom-by-atom until full evaporation of the surface layer is reached (i.e., after about 0.5 ps; see Figure 7). Then it stops for 0.7 ps as the previous surface layer has been completely removed and a new surface layer is exposed. The cohesive energy is again larger than for an incomplete surface and it has to gain an additional amount of energy after which the process of atom-by-atom evaporation occurs again for the new surface layer.

Our results indicate that the layer-by-layer evaporation is observed for all three crystals at low fluences, but it is more obvious (and the fluence range is wider) for Ni. The reason is that Ni has a low heat conductivity and its electron−phonon coupling parameter is an order of magnitude higher than for Au and Cu, so the energy transfer occurs more rapidly and is more localized.

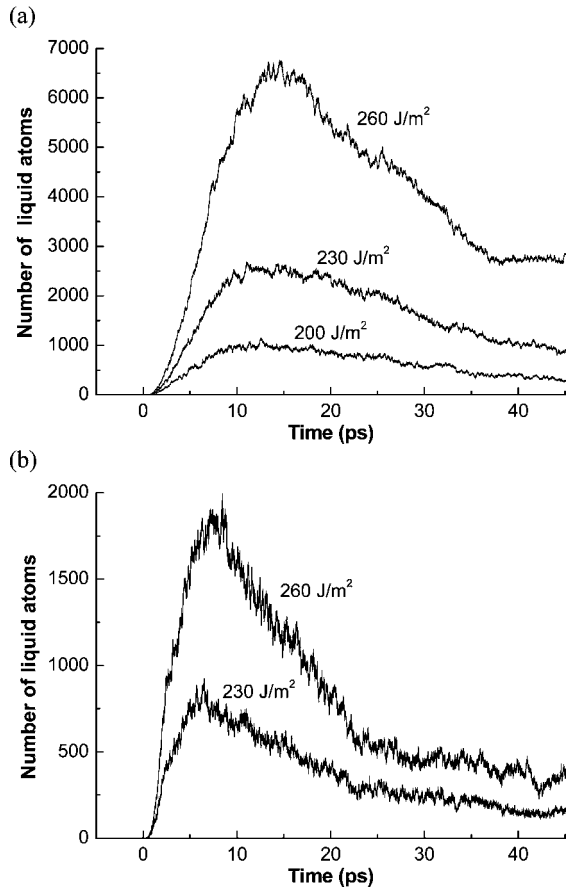

Figure 8. The number of liquid atoms vs time in Au (a) and Cu (b) for different absorbed fluences. The total number of atoms in the case of Au is 96 000, and it is 108 000 for the case of Cu.

The observed layer-by-layer evaporation is an indication that the vaporization happens from the solid phase rather than from the liquid phase, since there are no clear atomic layers in a liquid. The theoretically predicted kind of evaporation is in good agreement with experimental indications of a direct solid−vapor transition observed in femtosecond laser treatment of steel.[47] This means that when vaporization occurs, which happens mostly in the first 20 ps, a full liquid region at the surface is not formed yet. This leads to the belief that for the time scales under consideration, a definition of a liquid and solid phase is not a realistic representation of the occurring physical processes, and a continuum model should account for lattice distortion rather than for an actual solid to liquid phase transition. Furthermore, for evaporation a kinetic equation that describes a direct solid to vapor transition might be the best approach. Unfortunately, to our knowledge an equation that describes these processes is not known yet.

Figure 8 shows the amount of liquid atoms for Au and Cu at different laser fluences. Note that, as mentioned above, melting is negligible for Ni, hence the number of liquid atoms is very small at all fluences studied. It is seen that the amount of liquid atoms is larger for Au than for Cu. As mentioned in the Introduction, the main difference between these two metals is their density and their thermal expansion coefficient. However, the amount of evaporated material is quite similar for Au and Cu. The criterion based on a strict local order parameter when defining the liquid state could also be a reason for this large difference. Therefore Figure 8 should be used to study the temporal evolution more than the absolute amount of liquid material.

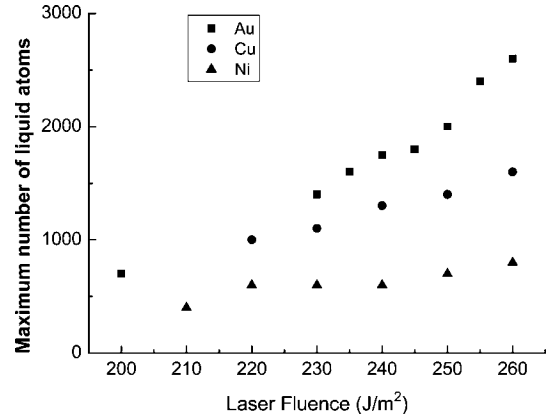

Figure 9. The maximum number of liquid atoms for ultrashort pulsed laser irradiation of different absorbed fluences for Au, Cu, and Ni.

The maximum number of liquid atoms is plotted as a function of absorbed fluence in Figure 9 for the three different metals. It is clear that the Au target is the most affected by the laser pulse, as the number of liquid atoms is higher, as was also obvious from Figure 8 above. The number of liquid atoms in the case of Ni is very low. This is due to the larger value of the electron−phonon coupling, which almost immediately removes the energy of the lattice and the electron subsystem by vaporization.

The initial intention of our study was to use MD-simulations to obtain a relation between the melting temperature and the melting front velocity, as was previously done by Jackson in ref 8. A melting front position was calculated based on the number of liquid atoms, and the temperature in a grid cell centered to the melting front position was considered as the melting temperature. The corroboration of the theory is not an easy task. The statistical nature of temperature and, to a lesser extent, the lack of a good definition of a clear melting front complicates the calculation. Nevertheless, using various filtering techniques, the results obtained by the MD-simulations did show that there is no clear relation between the melting temperature and the velocity of the melting front. The observed differences might be due to pressure effects, which are not included in the phenomenological theory. Hence, the inapplicability of the currently accepted superheating theory for ultrashort pulsed laser-induced melting does emphasize the need for combined continuum-MD models to study the laser-induced phase transitions in detail.

4. Conclusions

A combined atomistic-continuum model was used to study ultrashort (100 fs fwhm) pulsed laser-induced melting in Au, Cu, and Ni. At low fluences, a kind of layer-by-layer evaporation was observed. This direct solid to vapor transition might be a more realistic view of the evaporation process, especially for metals with high electron−phonon coupling, such as Ni. The results show that the amount of molten material remains very limited under the conditions studied. Because of the implementation of a moving boundary between the MD-box and the continuum part, the electron temperature gradient should be negligible when new cells are added. It was also demonstrated that the currently accepted superheating theory is not applicable for ultrashort pulsed laser-induced heterogeneous melting. This and the lack of an acceptable kinetic theory for homogeneous nucleation of liquid regions emphasizes the need for combined MD-continuum modeling to investigate ultrashort pulsed laser-induced phase transitions.

Acknowledgment. A.D. gratefully acknowledges Professor M. Hou (ULB, Brussels) for the basic MD-code that was modified further for the laser-induced melting processes. W.W. and A.D. are thankful to Professor L.V. Zhigilei for useful discussions and advices. The calculations were performed on the CALCUA computing facility of the University of Antwerp. This work was supported by the Belgian Science Policy (IAP).

References and Notes

(1) Bäuerle, D. *Laser Processing and Chemistry*; Springer-Verlag: Berlin, 2000.
(2) *Pulsed Laser Deposition of Thin Films*; Chrisey, D. B., Hubler, G. K., Eds.; Wiley-Interscience: New York, 1994.
(3) Jersch, J.; Demming, F.; Hildenhagen, J.; Dickmann, K. *Opt. Laser Technol.* **1997**, *29*, 433.
(4) Korte, F.; Serbin, J.; Koch, J.; Egbert, A.; Fallnich, C.; Ostendorf, A.; Chichkov, B. N. *Appl. Phys. A: Mater. Sci. Process.* **2003**, *77*, 229.
(5) Anisimov, S. I.; Kapeliovich, B. L.; Perel'man, T. L. *Sov. Phys. JETP* **1974**, *39*, 375.
(6) Chowdhury, I. H.; Xu, X. *Numer. Heat Transfer, Part A* **2003**, *44*, 219.
(7) Zhang, Y.; Chen, J. K. *Appl. Phys. A: Mater. Sci. Process.* **2007**, *88*, 289.
(8) Jackson, K. *Int. Sci.* **2002**, *10*, 159.
(9) Turnbull, D. *Solid State Phys.* **1956**, *3*, 225.
(10) Wei, J.; Sun, Z.; Zhang, F.; Xu, W.; Wang, Y.; Zhou, F.; Gan, F. *Chem. Phys. Lett.* **2004**, *392*, 415.
(11) Rethfeld, B.; Sokolowski-Tinten, K.; von der Linde, D.; Anisimov, S. I. *Phys. Rev. B* **2002**, *65*, 092103.
(12) Itina, T.; Hermann, J.; Delaporte, Ph.; Sentis, M. *Thin Solid Films* **2004**, *453*−*454*, 513.
(13) Volkov, A. N.; Zhigilei, L. V. *J. Phys.: Conference Series* **2007**, *59*, 640.
(14) Ivanov, D. S.; Zhigilei, L. V. *Phys. Rev. B* **2003**, *68*, 064114.
(15) Duff, W.; Zhigilei, L. V. *J. Phys.: Conf. Ser.* **2007**, *59*, 413.
(16) Lin, Z.; Johnson, R. A.; Zhigilei, L. V. *Phys. Rev. B* **2008**, *77*, 214108.
(17) Ivanov, D. S.; Zhigilei, L. V. *Phys. Rev. Lett.* **2007**, *98*, 195701.
(18) Häkkinen, H.; Landman, U. *Phys. Rev. Lett.* **1993**, *71*, 1023.
(19) Xu, X.; Cheng, C.; Chowdhury, I. H. *J. Heat Transfer* **2004**, *126*, 727.
(20) Amoruso, S.; Bruzzese, R.; Wang, X.; Nedialkov, N. N.; Atanasov, P. A. *J. Phys. D: Appl. Phys.* **2007**, *40*, 331.
(21) Yamashita, T. *Fusion Eng. Des.* **2006**, *81*, 1695.
(22) Lin, Z.; Zhigilei, L. V.; Celli, V. *Phys. Rev. B* **2008**, *77*, 075133.
(23) Anisimov, S. I.; Rethfeld, B. *Proc. SPIE* **1997**, *3093*, 192.
(24) White, G. K.; Collocott, S. J. *J. Phys. Chem. Ref. Data* **1984**, *13*, 4.
(25) Swope, W. C.; Andersen, H. W.; Berens, P. H.; Wilson, K. R. *J. Chem. Phys.* **1982**, *76*, 1.
(26) Cleri, F.; Rosato, V. *Phys. Rev. B* **1993**, *48*, 22.
(27) Ackland, G. J.; Vitek, V. *Phys. Rev.* **1990**, *41*, 10324.
(28) Foiles, S. M.; Baskes, M. I.; Daw, M. S. *Phys. Rev. B* **1986**, *33*, 7983.
(29) Johnson, R. A. *Phys. Rev. B* **1989**, *39*, 12554.
(30) Johnson, R. A. *Phys. Rev. B* **1990**, *41*, 9717.
(31) Owen, E. A.; Williams, R. W. *Proc. R. Soc. London, Ser. A* **1947**, *188*, 509.
(32) Flinn, P. A.; McManus, G. M.; Rayne, J. A. *Phys. Rev.* **1961**, *123*, 829.
(33) Chipman, D. R.; Paskin, A. *J. Appl. Phys.* **1959**, *30*, 1992.
(34) Simerska, M. *Acta Crystallogr.* **1961**, *14*, 1259.
(35) Wilson, R. H.; Skelton, E. F.; Katz, J. L. *Acta Crystallogr.* **1966**, *21*, 635.
(36) Adelman, S.; Doll, J. *J. Chem. Phys.* **1976**, *64*, 2375.
(37) Haberland, H.; Insepov, Z.; Moseler, M. *Phys. Rev. B* **1995**, *51*, 11061.
(38) Allen, M. P.; Tildesley, D. J. *Computer Simulation of Liquids*; Clarendon: Oxford, 1987.
(39) Van Hoof, T.; Dzhurakhalov, A.; Hou, M. *Eur. Phys. J. D* **2007**, *43*, 159.
(40) Morris, J. R.; Song, X. *J. Chem. Phys.* **2002**, *116*, 9352.
(41) Rethfeld, B.; Sokolowski-Tinten, K.; von der Linde, D.; Anisimov, S. I. *Appl. Phys. A: Mater. Sci. Process.* **2004**, *79*, 767.
(42) Ashitkov, S. I.; Agranat, M. B.; Kondratenko, P. S.; Anisimov, S. I.; Fortov, V. E.; Temnov, V. V.; Sokolowski-Tinten, K.; Rethfeld, B.; Zhou, P.; von der Linde, D. *JETP Lett.* **2002**, *76*, 461.
(43) Ivanov, D. S.; Zhigilei, L. V. *Phys. Rev. Lett.* **2003**, *91*, 105701.
(44) Zhigilei, L. V.; Ivanov, D. S.; Leveugle, E.; Sadigh, B.; Bringa, E. M. *Proc. SPIE* **2004**, *5448*, 505.
(45) Sokolowski-Tinten, K.; Blome, C.; Dietrich, C.; Tarasevitch, A.; Horn von Hoegen, M.; von der Linde, D.; Cavalleri, A.; Squier, J.; Kammler, M. *Phys. Rev. Lett.* **2001**, *87*, 225701.
(46) Wang, X.; Xu, X. *J. Heat Transfer* **2002**, *124*, 265.
(47) Nolte, S.; Kamlage, G.; Bauer, T.; Korte, F.; Fallnich, C.; Ostendorf, A.; von Alvensleben, F. *LaserOpto* **1999**, *31*, 72.

JP907385N